JOURNAL OF MATERIALS SCIENCE 23 (1988) 3447–3454

The effect of carbon on the high temperature oxidation of Fe–31Mn–9Al–0.87C alloy

C. J. WANG, J. G. DUH
Department of Materials Science and Engineering, National Tsing Hua University, Hsinchu, Taiwan, ROC

The alloy with the composition Fe–31Mn–9Al–0.87C was employed to investigate the effects of carbon on the oxidation behaviour at 800, 900 and 1000° C in dry air. Electron and optical microscopy were applied to examine the morphology and elemental redistribution in the oxide scale. Oxidation kinetics of the alloy oxidized at 800 and 900° C exhibited three-stage and two-stage parabolic rate laws, respectively. For the alloy oxidized at 1000° C, a carbon-induced breakaway three-stage oxidation mechanism developed. The carbon addition had a detrimental effect on the oxidation resistance and resulted in a porous initial oxide layer, which was favourable to the oxidation of manganese as well as the formation of a uniform and bulky oxide. As the oxidation temperature was increased, the diffusion rates of the metallic elements and the healing ability of oxide scales were enhanced. However, when the carbon content in alloy was above the saturation value, a breakaway scaling may have occurred due to the carbon-induced oxidation.

1. Introduction

The Fe–Al alloy is well known to have excellent high-temperature oxidation resistance due to the formation of the protective α-Al_2O_3 layer during the oxidation process. This alloy is, however, brittle and has poor mechanical properties because of its ferrite microstructure [1, 2]. The development of Fe–Mn–Al–C alloy has proceeded from this aspect by the addition of manganese and carbon to stabilize the austenite phase and improve mechanical properties [3, 4]. Previous works have concentrated on the austenitic Fe–30Mn–9Al–1C alloys in the study of the phase stability, mechanical property and corrosion resistance [5–9]. However, no Al_2O_3 or only a discontinuous Al_2O_3 layer was observed in this austenitic alloy [10, 11]. Recently, other alloying elements, such as silicon, chromium, nickel, copper and zirconium, have been introduced to improve the oxidation resistance [10–15]. More recently, the influence of carbon on the oxidation of Fe–Al–C alloys was investigated with the aid of kinetics and carbide redistribution studies [16–18]. It was reported that the addition of carbon had a detrimental effect on the oxidation resistance [16], and the oxidation behaviour was dominated by the carbide stability and the diffusion rate of metallic elements at different temperatures [17, 18]. In addition, it was indicated that the manganese stabilized the carbide and retarded the diffusion of carbon during oxidation [19]. For the Fe–Mn–Al system, the oxidation behaviour has also been investigated [20, 21]. Jackson and Wallwork [21] reported that the austenitic phase in the alloy was detrimental to the oxidation resistance due to the formation of manganese oxide nodules for the alloy containing in excess of 25 wt % manganese and 9 wt % aluminium. The oxidation of Fe–Mn–Al–C alloy with various carbon contents ranging from 0.3 to 1.3 wt % at 800° C was also studied [22]. It was observed that the oxidation kinetics were enhanced by increasing carbon content. However, the correlation between carbon and manganese during the high-temperature oxidation and the oxidation mechanism of the Fe–Mn–Al–C alloys has not been investigated. The purpose of this research was to study the effect of carbon on the high-temperature oxidation of the Fe–31Mn–9Al–0.87C alloy with emphasis on the influence of manganese on the migration of carbon during oxidation as well as the carbon-influenced oxidation at various temperatures. The morphology of the oxide scale was examined by scanning electron and optical microscopy. The concentration profiles of the elements were evaluated through quantitative analysis in an electron microprobe. The role of carbon in the oxidation process is discussed in terms of the kinetic evolution and morphology development. In addition, comparisons of the oxidation behaviour of Fe–Mn–Al–C, Fe–Al–C and Fe–Mn–Al is also made.

2. Experimental procedure

The chemical composition of the alloy employed in this study is listed in Table I. The alloy was prepared from high-purity materials and melted in an argon shield induction furnace. The ingot was forged at 1200° C with 75% reduction and then homogenized at 1200° C for 11 h. After surface finishing, the alloy was then rolled with 90% reduction to 2.3 mm thickness. In order to eliminate the grain growth during oxidation experiments and also to retain the carbon in the solid solution state, the alloy was annealed at 1150° C for 50 h in a tube furnace under a protective argon

0022–2461/88 $03.00 + .12

TABLE I Chemical compositions (wt %) of the alloy employed in this study

Mn	Al	C	Fe
31.18	8.69	0.87	Bal.

atmosphere. Austenite was the only phase present for the alloy after annealing and the grain size was calculated to be 200 μm. Specimens were cut into 2 mm × 4 mm × 8 mm for kinetic and morphological studies. For X-ray identification the specimen size was 2 mm × 10 mm × 20 mm in dimension. All samples were abraded and polished to 0.05 μm alumina powder, and washed ultrasonically in alcohol after the polishing process.

The temperatures for oxidation experiments were chosen as 800, 900 and 1000° C. The oxidation time ranged from 20 min to 24 h. The atmosphere employed was dry air with a flow rate of 200 $cm^3 min^{-1}$. Oxidation kinetics of alloy oxidized for 24 h were recorded continuously with a computerized thermogravimetric analyser (TGA, TGD-5000 Ulvac/Sinku Riko, Japan). All samples were air cooled after the oxidation experiments. Possible phases present in the specimen were identified with the X-ray diffractometer. The morphologies of the oxide and alloy substrate were examined by both the optical microscopy (OM) and scanning electron microscopy (SEM). Elemental redistribution was detected through an X-ray map technique with a computerized electron microprobe (Jeol JCXA-733). In addition, the quantitative analysis of the concentration for iron, manganese and aluminium was performed with the aid of a ZAF-corrected program.

3. Results

3.1. Oxidation kinetics

Fig. 1 shows the typical oxidation kinetics of the alloy oxidized at 800, 900 and 1000° C. It seems that the increase in weight is not simply proportional to the temperature increase for the 24 h oxidation. The lowest weight gains are found for the oxidation at 900° C, but not at 800° C. Fig. 2 represents the Arrhenius plot, i.e. square of weight gain per unit area against time, for the sample oxidized at 800° C. Using the Arrhenius equation, the parabolic rate constants were calculated and are listed in Table II. There exist different parabolic rates at 800° C as seen in Fig. 2. The first stage of oxidation takes place during the first 2 h, and the parabolic rate constant is represented as K_{p1}. After the first stage, oxidation with a higher oxidation rate, K_{p2},

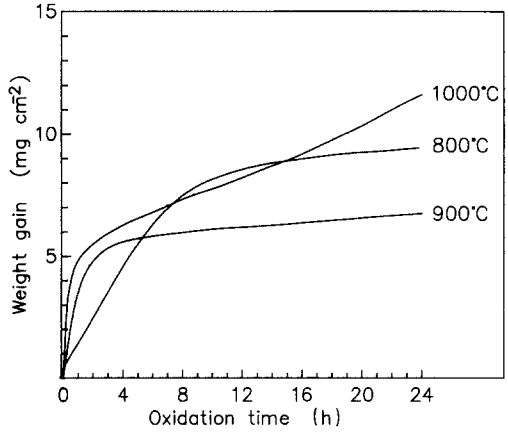

Figure 1 Oxidation kinetics of Fe–31Mn–9Al–0.87C alloy oxidized from 800 to 1000° C in dry air.

occurs. As the oxidation time increases to 14 h, a steady state oxidation with lower parabolic rate, K_{p3}, shows up.

Fig. 3 is the Arrhenius plot of the alloy oxidized at 900° C, which exhibits two distinct parabolic rates. The first stage of oxidation takes place within the initial 2 h with a higher parabolic rate. As oxidation time increases to 4 h, the second stage of oxidation occurs and exhibits a steady state growth of oxides with the lowest parabolic rate observed in this study.

The Arrhenius plot for the specimen oxidized at 1000° C is presented in Fig. 4. Three different oxidation rates are observed, but with different oxidation behaviour from that at 800° C. Similar to the oxidation at 900° C, a fast first stage and a healing second stage of oxidation are observed for the oxidation time less than 14 h. However, a breakaway oxidation occurs after the second stage oxidation, as seen in Fig. 4.

3.2. Morphological studies

Fig. 5 shows the surface morphology of the sample oxidized at 800° C for 20 min in which the oxide protrusions are visible. No spalling is observed when the sample is air cooled to room temperature. The oxide scale and protrusions are identified as (Fe, $Mn)_2O_3$ and (Fe, $Mn)_3O_4$, respectively, on the basis of the X-ray diffraction result. The surface morphology and oxide distribution of the sample oxidized for 1 h are similar to those for 20 min. However, small amounts of oxide scale are spalled off during cooling, with the cavity left as shown in Fig. 6.

The spalled oxide after 24 h oxidation is identified as Mn_2O_3, Fe_2O_3 and a little (Fe, $Mn)_3O_4$. Figs 7a to

TABLE II The parabolic rate constants ($mg^2 cm^{-4} sec^{-1}$) for the alloy oxidized at 800, 900 and 1000° C

Temperature	K_{p1}	K_{p2}	K_{p3}
800	(7.04 ± 0.98) × 10^{-4} (< 2 h)	(2.35 ± 0.03) × 10^{-3} (2–9 h)	(3.13 ± 0.10) × 10^{-4} (14–24 h)
900	(3.36 ± 0.20) × 10^{-3} (< 2 h)	(1.70 ± 0.01) × 10^{-4} (8–24 h)	
1000	(6.51 ± 1.39) × 10^{-3} (< 1 h)	(1.01 ± 0.01) × 10^{-3} (2–14 h)	(1.87 ± 0.02) × 10^{-3} 18–24 h)

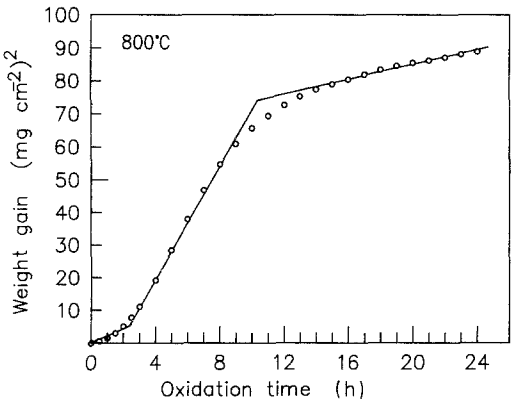

Figure 2 Arrhenius plot of the alloy oxidized at 800° C in dry air.

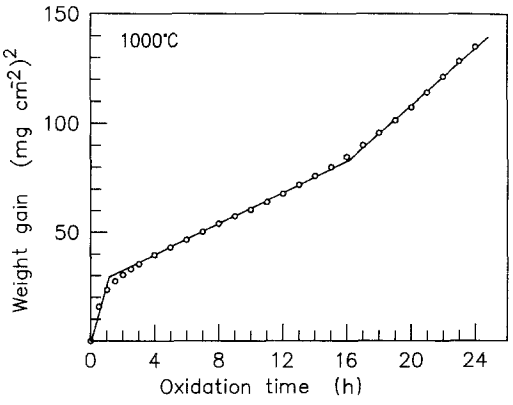

Figure 4 Arrhenius plot of the alloy oxidized at 1000° C in dry air.

d represents the SEM image, and X-ray maps of aluminium, manganese and iron, respectively, for the alloy oxidized at 800° C for 24 h. Two distinct oxide layers are visible as shown in Fig. 7a. The exterior layer is caused by the outward diffusion of the cation, and a secondary ferrite layer is observed between the inner oxide layer and the γ matrix. The elemental concentration profiles with respect to the trace line in Fig. 7a are indicated in Fig. 8. On the basis of the results shown in Figs 7a to d and 8, it is found that the outermost region in the oxide scale is rich in manganese, while aluminium is enriched in the inner layer. Together with the X-ray diffraction data, the oxide scale at 800° C for 24 h is further identified as Mn_2O_3, (Fe, $Mn)_2O_3$, Fe_2O_3, (Fe, $Mn)_3O_4$ and (Fe, Mn)Al_2O_4 from the outermost scale to the inner layer.

For the alloy oxidized at 900° C for 20 min, the oxide is determined to be a manganese enriched compound, such as (Fe, $Mn)_2O_3$ and (Fe, $Mn)_3O_4$, $MnAl_2O_4$ and a little MnO. Some extents of (Fe, $Mn)_2O_3$ and (Fe, $Mn)_3O_4$ are spalled off during cooling. Figs 9a and b represent the SEM images for the sample oxidized at 900° C for 20 min and 1 h, respectively. However, little cavitation can be found in the spalled region, as indicated in Fig. 9b. As seen in Fig. 9a, many cavities are observed in the outer region with (Fe, $Mn)_2O_3$. Cavities with large sizes are also observed in the middle layer oxide with (Fe, $Mn)_3O_4$. As oxidation proceeds to 24 h, (Fe, $Mn)_2O_3$ and (Fe, $Mn)_3O_4$ are spalled off in the cooling process. Fig. 10 shows the SEM image and the elemental X-ray map of the oxide at 900° C for 24 h after spalling. A secondary ferrite layer is observed between the oxide and γ matrix, as similar to the case at 800° C. Relatively dense aluminium is found in the innermost oxide layer, while manganese and a small amount of iron scatter in the residual region of this oxide layer. The unspalled oxide is further identified to be mostly $MnAl_2O_4$ with some Al_2O_3 and (Fe, $Mn)_3O_4$.

Fig. 11 shows the SEM image of the oxide for the sample oxidized at 1000° C for 20 min, which is a relatively loose morphology. Mn_2O_3 is not present in this case and the major oxides are (Fe, $Mn)_3O_4$, with a little MnO and $MnAl_2O_4$. For 24 h oxidation, the oxides in the outer layer, i.e. (Fe, $Mn)_3O_4$, Fe_2O_3 with a little $MnAl_2O_4$, are spalled off during cooling. Two regions with distinct morphology are observed in the spalled specimen. A nearly planar interface between the secondary ferrite layer and austenite matrix is found, as seen in Fig. 12a. Fine stringers of Fe_3AlC_x are located in the grain boundaries and also dispersed in the ferrite grain near the oxide layer. The elemental redistributions, as shown in Figs 12b to d, indicate that the oxide layer is rich in aluminium with a small amount of manganese. The X-ray diffraction results show that the outer region is $MnAl_2O_4$ and the aluminium-rich layer is Al_2O_3.

Fig. 13 represents the concentration profiles of the metallic elements corresponding to the trace line in Fig. 12a. It is apparent that the manganese is depleted in the region between the γ matrix and the oxide layer.

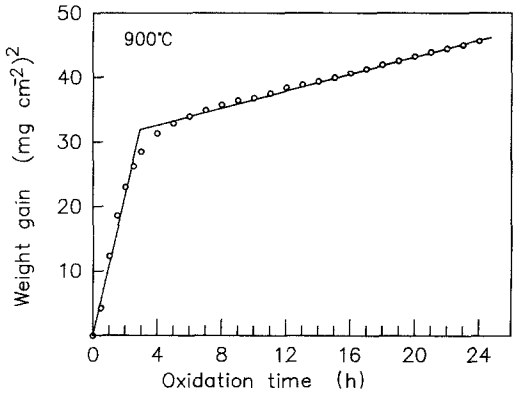

Figure 3 Arrhenius plot of the alloy oxidized at 900° C in dry air.

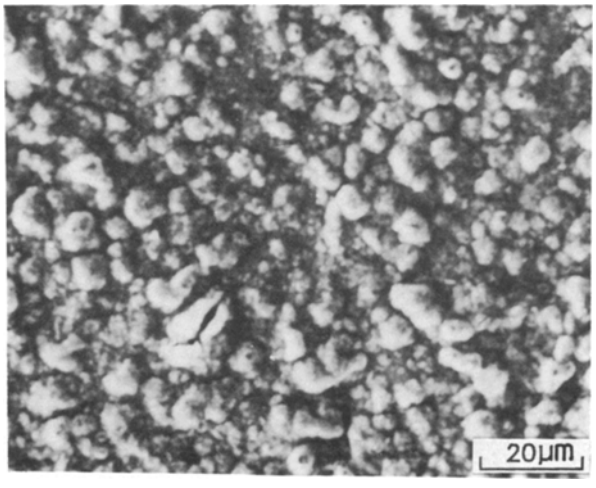

Figure 5 Surface morphology of the alloy oxidized at 800° C for 20 min, oxide protrusions are uniformly distributed.

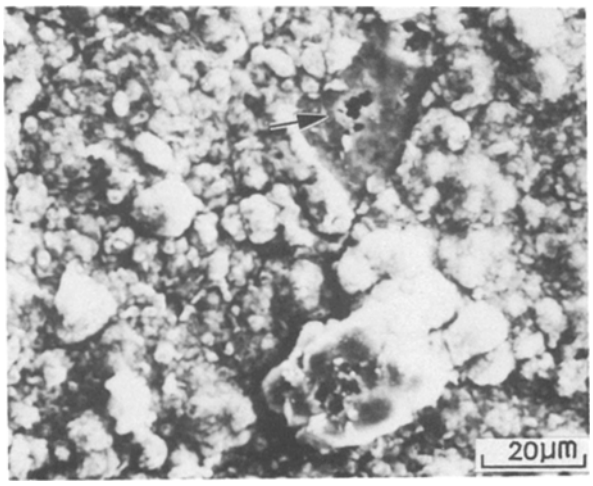

Figure 6 Surface morphology of the alloy oxidized at 800° C for 1 h, the arrow points to the cavity in the inner oxide layer.

The other region with different morphology is related to the large and broad oxide nodule developed as indicated in Fig. 14. Beneath the oxide nodule, the width of the ferrite layer is less thick, and numbers of carbides are also reduced. With the presence of the oxide nodule, large voids are visible. The oxides in the nodule are mostly $(Fe, Mn)_3O_4$ with a little Fe_2O_3. In addition, some fragments of $MnAl_2O_4$, the dark phase as seen in Fig. 14, are dispersed in the $(Fe, Mn)_3O_4$ nodule. It should be pointed out that with the occurrence of breakaway oxidation, there exists some degree of scattering for the TGA data when a broad nodule is observed after oxidation.

4. Discussion

Recently, high-temperature oxidation of Fe–Al–C alloys ranging from 500 to 1100° C was reported [16–18], which indicated that the oxidation behaviour was dependent on the temperature-influenced carbide stability, aluminium content and the elemental diffusion rate. At higher temperature, the elemental diffusion rate is accelerated. If the aluminium content in the alloy is sufficient, aluminium would oxidize to form Al_2O_3 or other aluminium-rich oxides, which in turn retard the participation of carbon in the oxidation process. On the other hand, with deficient aluminium content in the alloy, the unstability of the carbide at high temperature would tend to induce decarburization, which could decelerate the formation of aluminium oxide and thus the oxidation resistance of the alloy was degraded. For oxidation at lower temperature, the carbide is more stable and the elemental diffusion rate is also lower. Hence, it is difficult for protective aluminium-rich oxide to form, or internal oxidation takes place instead. Several studies have focused on the oxidation behaviour of Fe–Al–C with addition of manganese [10, 11, 19]. Because of the low dissociation pressure of MnO, the high vapour pressure and oxidation rate of manganese, the overall oxidation behaviour is dominated by the oxidation of manganese [11, 21, 23]. Since manganese acts as the

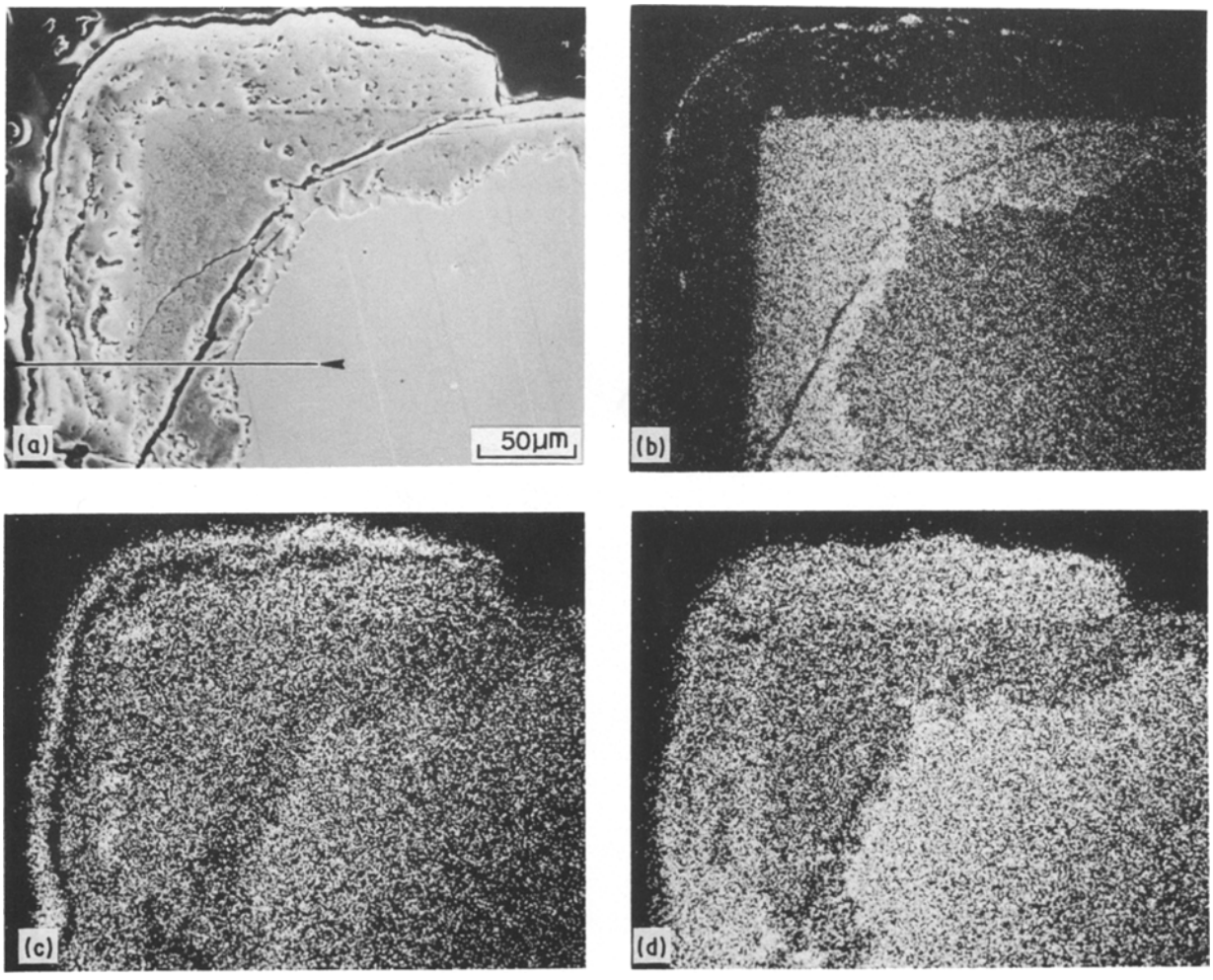

Figure 7 Cross-sectional view of the alloy oxidized at 800° C for 24 h: (a) SEM image, (b) Al X-ray map, (c) Mn X-ray map, (d) Fe X-ray map.

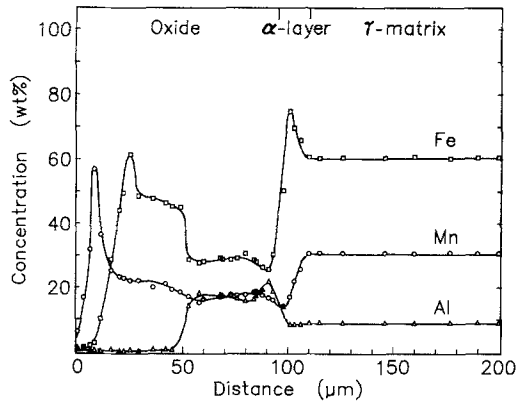

Figure 8 Concentration profiles of metallic elements of the alloy oxidized at 800° C for 24 h.

austenite stabilizer and also the carbide former, the addition of manganese in Fe–Al–C alloy tends to promote the austenitic phase, and at the same time degrades the role of carbon in the oxidation [19, 24].

During the initial stage of oxidation of Fe–Mn–Al–C at 800° C in this study, MnO and FeO are formed due to the outward diffusion of cations and a little Al_2O_3 is nucleated by the inward diffusion of oxygen. Because of the interaction between manganese and carbon as described above, only the carbon located adjacent to the alloy surface could be oxidized to CO or CO_2 and then evaporated. As 31 wt % Mn is sufficient to stabilize FeO [10, 19], MnO and FeO would form the solid solution oxide (Fe, Mn)O [10, 23], which is subsequently oxidized to (Fe, Mn)$_3O_4$ due to the presence of high oxygen partial pressure at 800° C. Because Mn_2O_3 exhibits a higher dissociation pressure, some of the Mn_3O_4 tends to be reoxidized to form Mn_2O_3 in the exterior of the scale. The participation of carbon in the initial oxidation leaves uniformly distributed cavities within the (Fe, Mn)O layer, which would provide an easy path for the migration of iron, manganese and oxygen, and thus forms a rather uniform oxide scale. Hence, a uniformly distributed Mn_2O_3 is formed along with the underlying (Fe, Mn)$_3O_4$, as shown in Fig. 5. It is reported that a dense and compact oxide could retard the oxidation of carbon [25]. As seen in Fig. 5, the oxide layer is rather dense and shows good adherence. This renders a relatively lower oxidation rate in the first stage, as indicated in Fig. 2.

As oxidation proceeds, more manganese migrates outwards, which decreases the drag force of manganese on carbon in the alloy matrix. The carbon activity is promoted due to the inner oxide layer formed by the inward diffusion of oxygen. As a result, the excess carbon enters the oxidation process and produces cavities on the surface of the specimen, as shown in Fig. 6. For longer oxidation times, the carbon in the alloy matrix may be oversaturated and a carbon-induced second stage oxidation occurs. It has been reported that the oxidation rate is enhanced with the participation of carbon [16–19, 22]. As indicated in Fig. 2, the second stage oxidation exhibits a higher oxidation rate, which implies that the residual carbon left in the first stage affects the oxidation behaviour during the second stage oxidation. The defects, such as cavities, produced by the oxidation of carbon, provide a fast oxidation route. The extensive migration of manganese towards the oxide scale promotes the relative aluminium contents near the alloy matrix and (Fe, Mn)Al_2O_4 is formed, as indicated in Figs 7 and 8. As manganese is depleted in the matrix near the oxide, a secondary ferrite layer is formed. Because the solubility of carbon in ferrite is low, the presence of ferrite acts as the barrier for diffusion, unless the oxidation chemical potential for P_{O_2} and/or the activity of carbon is sufficiently high for carbon to pass through the ferrite layer. With the existence of the diffusion barrier, the oxide in the inner layer is (Fe, Mn)$_3O_4$. If this occurs, carbon would fail to perturb the oxidation and one has the third stage oxidation which is characterized as the steady stage growth of (Fe, Mn)Al_2O_4.

As indicated in Figs 3, 9 and 10, the oxidation kinetics and morphologies for the alloy oxidized at 900° C are different from those oxidized at 800° C. This is attributed to the temperature-influenced metallic elemental diffusion rate and the carbide stability. Oxides of MnO, FeO, Al_2O_3 and CO are formed initially, and then further oxidized to (Fe, Mn)$_3O_4$ and Mn_2O_3. As large amounts of manganese aluminium participate in the oxidation, some MnO and Al_2O_3 form the spinel oxide, $MnAl_2O_4$. The thermodynamic

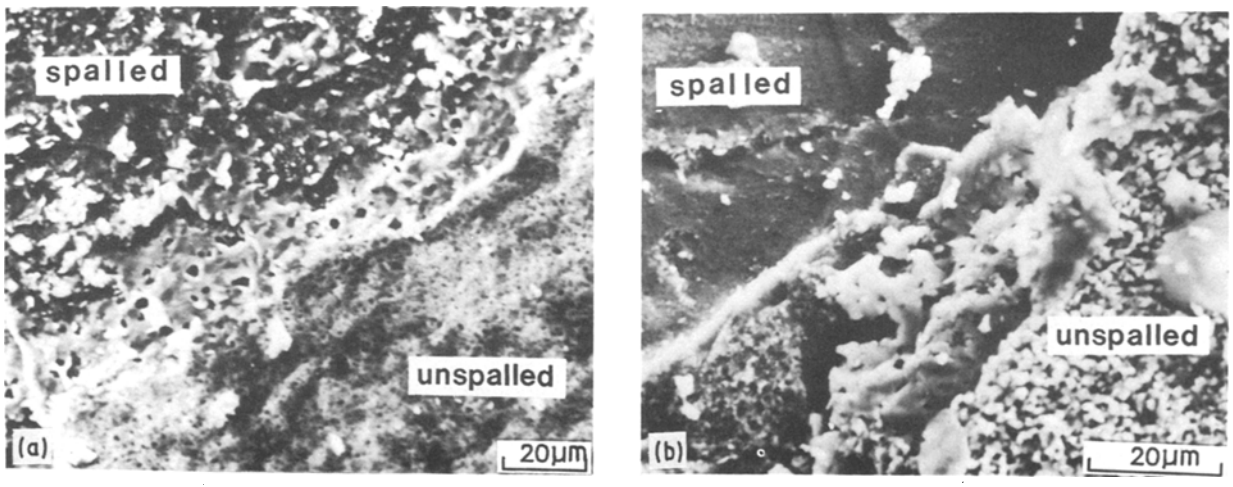

Figure 9 Surface morphology of the region containing spalled and unspalled oxides for the alloy oxidized at 900° C for (a) 20 min, (b) 1 h.

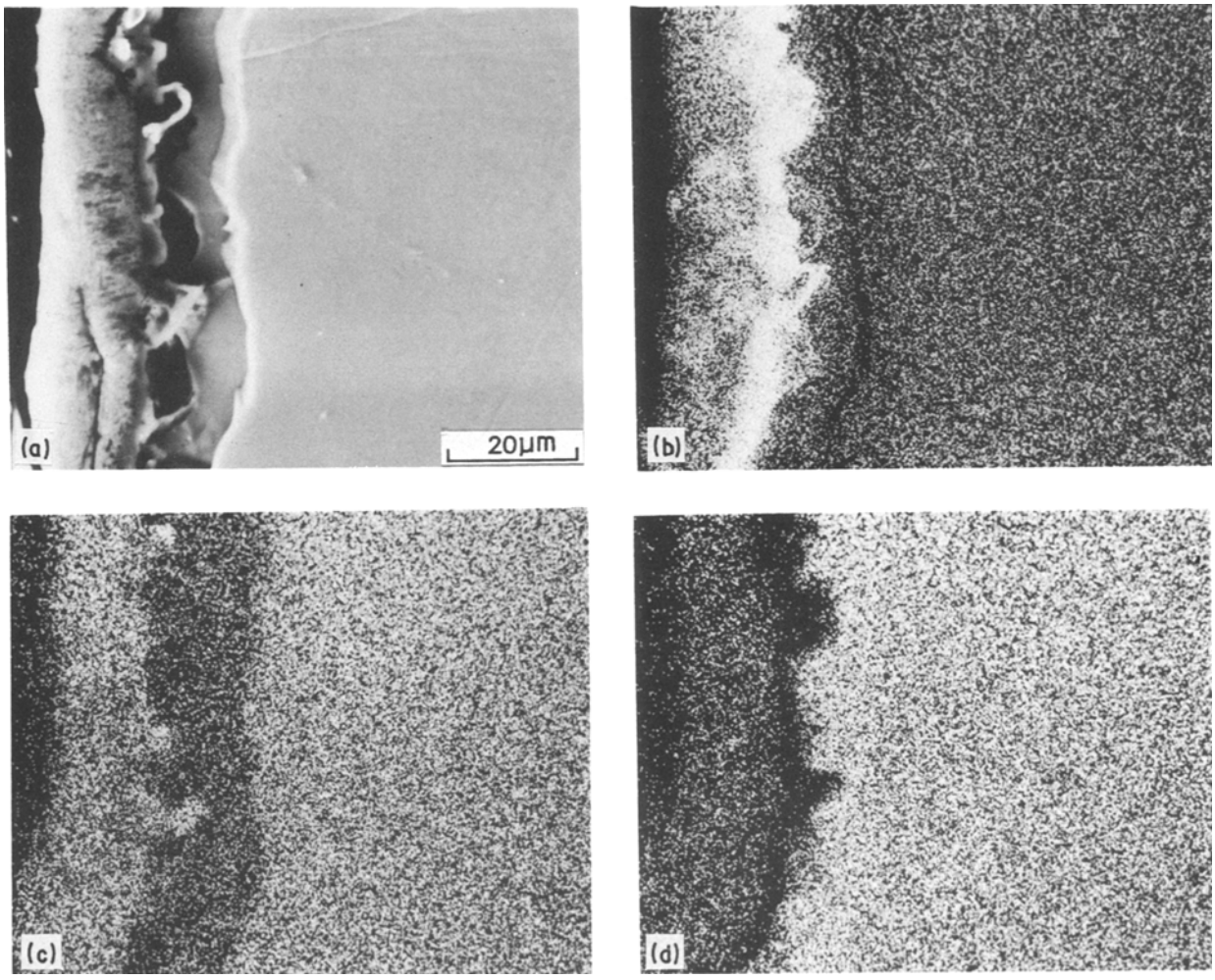

Figure 10 Cross-sectional view of the alloy oxidized at 900° C for 24 h: (a) SEM image, (b) Al X-ray map, (c) Mn X-ray map, (d) Fe X-ray map.

stability of the carbide $(Fe, Mn)_3AlC$ is degraded at 900° C compared to 800° C, hence more carbons are induced to participate in the initial oxidation and the oxidation rate is increased. This would leave cavities in the exterior of the oxide layer as shown in Fig. 9a, which is different from Fig. 5. Several large cavities are visible in the middle oxide layer, due to the fast cation diffusion rate caused by the higher temperature. It is believed that the cavitation is the result of accumulation of vacancies left by the outward diffusion of metallic ions, as manganese oxidizes from Mn_3O_4 to Mn_2O_3. At the matrix/oxide interface, the acceleration of the metallic element diffusion rate and the formation of the carbon-depleted layer in the initial oxidation time tend to promote the healing ability of the oxide. As a consequence, dense $MnAl_2O_4$ and Al_2O_3 are formed, as shown in Fig. 9b. Similar to the case at 800° C, the manganese depletion produces the secondary ferrite layer and $(Fe, Mn)_3AlC$ begins to precipitate in the alloy matrix. The oxidation rate is thus slowed down and turns to the second stage as shown in Fig. 10, due to the precipitation of $(Fe, Mn)_3AlC$, the formation of a ferrite layer and the healed protective aluminium-rich oxide layer. This feature could be verified by the Arrhenius plot as presented in Fig. 3 and the X-ray map of aluminium as seen in Fig. 10b.

The oxidation behaviour at 1000° C is similar to that at 900° C for the first two stages. The first stage is related to the carbon-induced oxidation, and then followed by the second healed stage. However, no Mn_2O_3 oxide is ever observed because it is thermodynamically unstable at 1000° C. During the initial oxidation, MnO, FeO and Al_2O_3 are formed, and the carbon near the surface of the specimen is depleted. Due to the carbon-induced oxidation and the fast growth of oxides at high temperature, higher oxidation kinetics is achieved as indicated in Fig. 4 and loose $(Fe, Mn)_3O_4$ oxide is formed at the outermost scale, as shown in Fig. 11. As oxidation progresses, the oxide layer is healed in the carbon-depleted region and the decarburization is thus retarded. With the presence of the porous oxide scale formed in the first stage, the preferential oxidation of manganese comes into effect and predominates the second stage oxidation, which exhibits a lower oxidation rate than the first, as indicated in Fig. 4. The stability of austenite is then degraded and the ferrite is formed, as seen in Figs 12 and 13. The residual carbon in the region is precipitated as Fe_3AlC_x in the grain boundaries and within the ferrite grains due to the fast depletion of manganese, as seen in Fig. 12a. However, if the inward growth of oxides comes into contact with the carbides or internal cracks caused by the stress resulting from the growth of oxides, the carbon in the carbide would be released into the oxidation process. This results in the breakaway oxidation. As the carbon content in the

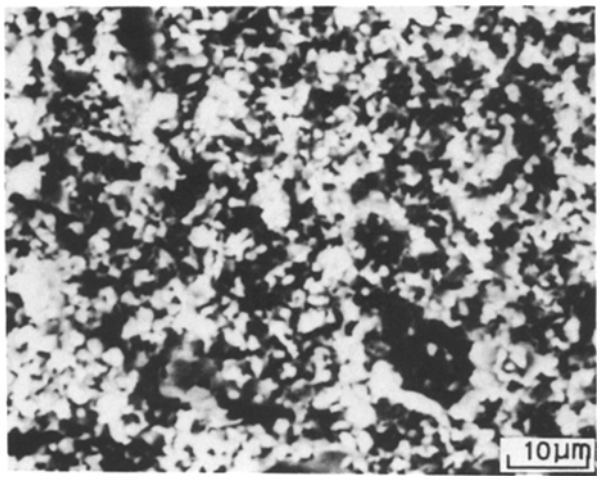

Figure 11 Surface morphology of the alloy oxidized at 1000° C for 20 min.

carbide is high, the degree of local breakaway oxidation induced by carbon is enhanced, compared to the first stage. Large oxide nodules are thus created and some of the healed oxides, such as $MnAl_2O_4$, formed during the second stage, are dispersed in the nodules as indicated in Fig. 14.

On referring to the oxidation studies of Fe–Al–C and carbon-free Fe–Mn–Al alloy, it is seen that the oxidation behaviour of Fe–31Mn–9Al–0.87C alloy is similar to that of Fe–Al–C alloys [16–18]. The major difference is that the oxidation of carbon could be retarded by the presence of manganese. More carbon can be dragged in to stay in the γ matrix by manganese, if the oxide layer is dense and well healed, as in the case of 900° C oxidation. The oxide formation in Fe–Mn–Al–C alloy in this study is basically identical to that of Fe–Mn–Al alloy [21]. However, the carbon-induced oxidation tends to perturb the compact integrity of the initial oxide layer and leaves cavities behind. This, in turn, provides easy path for the migration of the oxidants and results in the bulky oxide morphology rather than local nodules [21]. The resulting weight gain is much higher compared to the carbon-free Fe–Mn–Al alloy [21]. If the temperature is raised, and the oxide layer is well healed, manganese depletion occurs by preferential oxidation. The excess carbon would induce the breakaway oxidation, and the resulting oxide morphology is the large and broad nodules instead of the aluminium internal oxidation [10] or duplex oxide scale [21].

Based on the results in this study, it is found that carbon addition to Fe–Mn–Al alloy is, in fact, detrimental to the oxidation resistance. However, carbon is the essential element from the viewpoint of mechanical properties, as it is the austenite stabilizer for the enhancement of toughness [3, 4, 6, 8, 26]. Fairly good mechanical properties of the Fe–Mn–Al–C-based alloy have been reported [3, 4, 8]. Thus, it is desirable to prevent the carbon participation during oxidation for the practical application of the Fe–Mn–Al–C

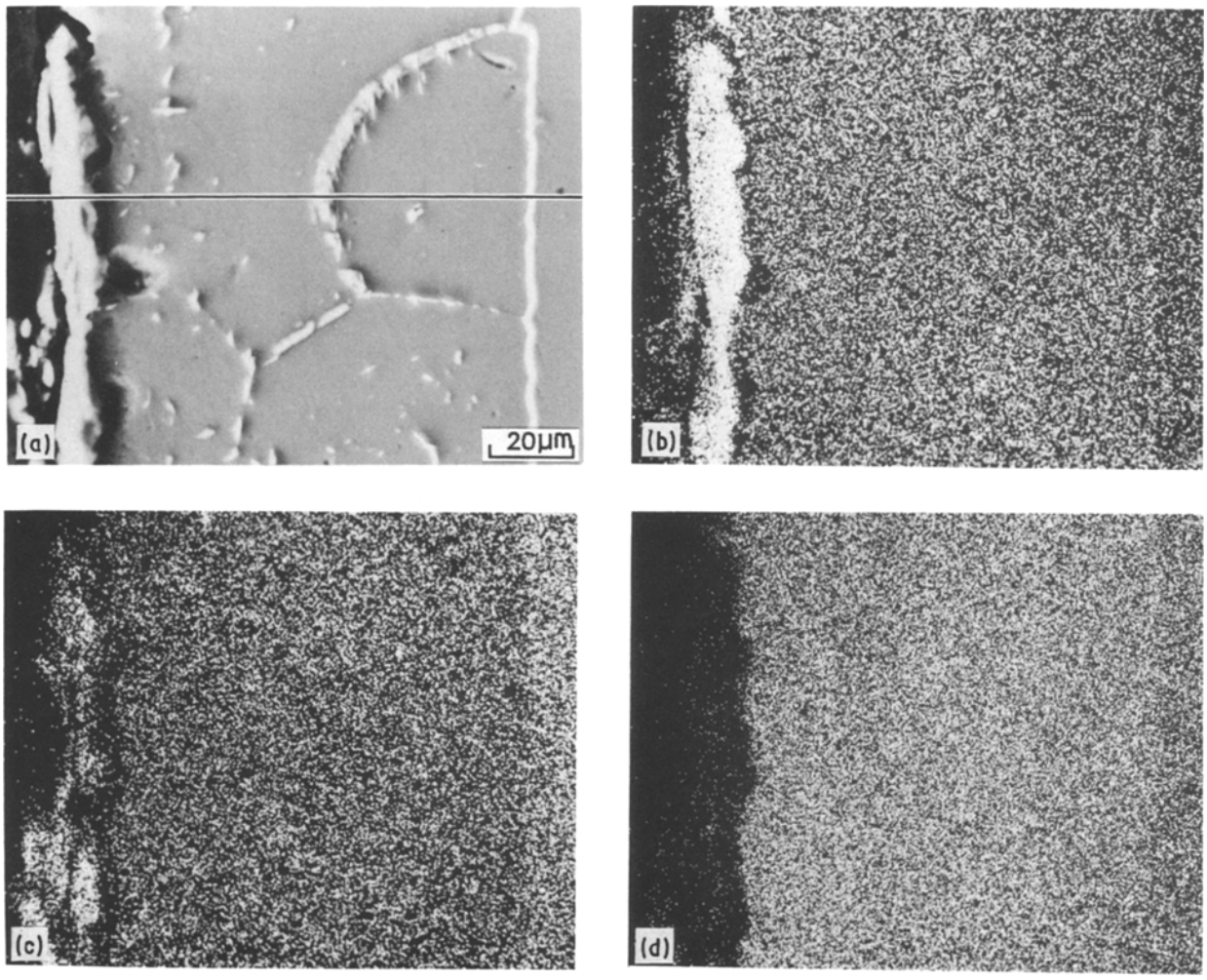

Figure 12 Morphology and elemental distribution of the alloy oxidized at 1000° C for 24 h: (a) SEM image, (b) Al X-ray map, (c) Mn X-ray map, (d) Fe X-ray map.

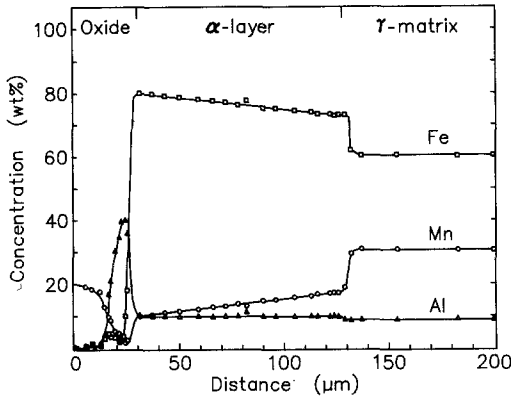

Figure 13 Concentration profiles of metallic elements of the alloy oxidized at 1000° C for 24 h.

alloys. This might be achieved by the addition of a carbide-former alloying element, such as chromium, to decelerate the decarburization [11, 12, 24]. Another alternative is to add silicon to stabilize MnO, and then to enhance the formation of α-Al_2O_3 [3–7, 10, 15]. However, silicon acts as the ferrite former, which is harmful to the mechanical properties [8]. It is argued that partial substitution of carbon by nitrogen might work with respect to the optimum achievement in both oxidation resistance and mechanical properties. Nevertheless, the formation of AlN [27] under such conditions should be taken into consideration.

5. Conclusions

1. For the Fe–31Mn–9Al–0.87C alloy oxidized at 800° C for 24 h, three distinct oxidation stages with different parabolic rates are observed. The first is the growth of Mn_2O_3 and $(Fe, Mn)_3O_4$, followed by carbon-induced oxidation. The steady state growth of $(Fe, Mn)Al_2O_4$ concludes the third stage of oxidation.

2. For the alloy oxidized at 900° C for 24 h, two distinct oxidation stages are visible. The carbon-induced oxidation takes place first, which is followed by the steady state growth of $MnAl_2O_4$.

3. For the alloy oxidized at 1000° C for 24 h, three distinct stages of oxidation are found. The first two are similar to those at 900° C. As the carbon from the Fe_3AlC_x in the secondary ferrite layer is induced into the oxidation, a breakaway oxidation occurs in the third stage.

4. The oxidation behaviour of Fe–Mn–Al–C alloy is similar to that of Fe–Al–C alloy, while the morphology of oxide formation in Fe–Mn–Al–C alloy resembles the Fe–Mn–Al alloy. The oxidation of carbon could be retarded by the presence of manganese, and more carbon is dragged by manganese into the alloy matrix, if the oxide layer is compact and well healed.

5. The carbon addition in the Fe–Mn–Al system appears to be detrimental to the oxidation resistance of the alloy, and results in a porous oxide layer. This favours the oxidation of manganese and the formation of rather uniform and bulky oxide scales.

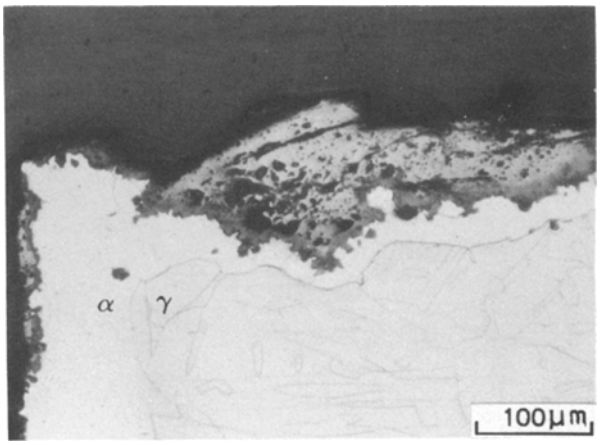

Figure 14 Cross-section view of broad oxide nodule for the alloy oxidized at 1000° C for 24 h; wavy α/γ interface is visible.

References

1. W. E. BOGGS, *J. Electrochem. Soc.* **118** (1971) 906.
2. N. G. SCHMAHL, H. BAUMANN and H. SCHENDS, *Arch. Eisenhuttenw.* **30** (1937) 161.
3. S. K. BANERJI, "An Update on Fe–Mn–Al Steels", Proceedings of the Workshop on "Conservation and Substitution Technology for Critical Materials", Vanderbilt University, Nashville, Tennessee, June 1981.
4. *Idem*, "The 1982 Status Report on Fe–Mn–Al Steels", presented at the Public Workshop on "Trends in Critical Materials Requirements for Steels of the Future-Conservation and Substitution Technology for Chromium", Vanderbilt University, Nashville, Tennessee, October 1982.
5. *Idem, Metal. Prog.* **113** (1978) 29.
6. R. WANG and F. H. BECK, *ibid.* **123** (1983) 72.
7. G. E. HALE and A. J. BAKER, in "Alternate Alloying for Environmental Resistance", edited by G. R. Smolik and S. K. Banerji (The Metallurgical Society, Warrendale, PA, USA, 1987) p. 67.
8. C. J. ALTSTETTER, A. P. BENTLEY, J. W. FOURIE and A. N. KIRKBRIDE, *Mater. Sci. Engng* **82** (1986) 13.
9. S. C. TJONG and N. J. HO, *ibid.* **91** (1987) 161.
10. J. P. SAUER, R. A. RAPP and J. P. HIRTH, *Oxid. Met.* **18** (1982) 285.
11. J. G. DUH, C. J. LIN, J. W. LEE and C. M. WAN, in "Alternate Alloying for Environmental Resistance", edited by G. R. Smolik and S. K. Banerji (The Metallurgical Society, Warrendale, PA, USA, 1987) p. 283.
12. J. G. DUH, C. J. WANG, C. M. WAN and B. S. CHIOU, *ibid.*, p. 291.
13. G. R. SMOLIK, J. E. FLINN, D. V. MILEY and G. E. KORTH, *ibid.*, p. 307.
14. C. H. KAO, C. M. WAN and M. T. JAHN, *ibid.*, p. 347.
15. R. WANG, M. J. STRASZHEIM and R. A. RAPP, *Oxid. Met.* **21** (1984) 71.
16. C. H. KAO and C. M. WAN, *J. Mater. Sci.* **22** (1987) 3203 in press.
17. *Idem, ibid.* **23** (1988) 894.
18. *Idem, ibid.* (1988) in press.
19. *Idem, ibid.* **23** (1988) 744.
20. B. K. LEE, Master Thesis, National Tsing Hua University, Taiwan, May (1983).
21. P. R. S. JACKSON and G. R. WALLWORK, *Oxid. Met.* **21** (1984) 135.
22. C. H. KAO, C. M. WAN and M. T. JAHN, in "Alternate Alloying for Environmental Resistance", edited by G. R. Smolik and S. K. Banerji (The Metallurgical Society, Warrendale, PA, USA, 1987) p. 299.
23. P. R. S. JACKSON and G. R. WALLWORK, *Oxid. Met.* **20** (1983) 1.
24. A. U. MALIK, *ibid.* **25** (1985) 233.
25. J. BAUD, A. FERRIER, J. MANENC and J. BENARD, *ibid.* **9** (1975) 69.
26. J. CHARLES, A. BERGHEZAN, A. LUTTS and P. L. DANCOISNE, *Metal. Prog.* **116** (1981) 71.
27. C. J. WANG and J. G. DUH, *J. Mater. Sci.* **23** (1988) 769.

Received 22 September 1987
and accepted 26 January 1988